Dark matter, collider searches and the early Universe

Farvah Mahmoudi

Univ. Lyon, Univ. Lyon 1, CNRS/IN2P3, Institut de Physique Nucléaire de Lyon, UMR5822, F-69622 Villeurbanne, France

E-mail: `nazila@cern.ch`

Abstract. Big-Bang nucleosynthesis (BBN) represents one of the earliest phenomena which can lead to observational constraints on the early Universe properties. Yet, it is well-known that many important mechanisms and phase transitions occurred before BBN. We will discuss the possibility to gain insight about the primordial Universe through studies of dark matter in cosmology, astroparticle physics and colliders. For this purpose we consider that dark matter is a thermal relic, and show that combining collider searches with dark matter observables can lead to strong constraints on the cosmological freeze-out period.

1. Introduction

Dark matter (DM) constitutes one of the strongest constraints on New Physics scenarios. However, DM detection searches suffer from large astrophysical uncertainties, namely on the DM distribution in the Galaxy and on cosmic ray propagation through the galactic medium. The calculation of the dark matter relic density also suffers from our lack of knowledge of early Universe phenomena. In the following we examine, in some detail, the impact of such uncertainties on the constraints on the minimal supersymmetric extension of the Standard Model (MSSM).

On the other hand, a reversed approach can be considered, in particular in the case of New Physics discoveries, to obtain constraints on the early Universe's properties. As an example of non-standard evolution, we consider models with a scalar field that may decay into beyond the Standard Model (BSM) particles. In any given BSM scenario, a deviation of the measured cold dark matter density from a calculation based on measurements of the model parameters and standard radiation dominated expansion would be a signature of novel phenomena in the very early Universe. One might argue that, if the calculated relic density is different from the measured dark matter density, the corresponding BSM scenario is disfavoured. Here, however, we propose to reverse this argument: if the calculated relic density is different from the measured dark matter density, it could be because of novel phenomena in the early Universe. This orthogonal point of view will become particularly important if new particles are discovered at colliders or in dark matter detection experiments: using dark matter observables, it is not possible to constrain BSM scenarios in isolation, but the constraints have to be applied simultaneously to a combination of BSM and cosmological scenarios.

2. Dark matter

2.1. Relic density

The dark matter abundance has been measured in the framework of the standard cosmological model, and the Planck Collaboration has provided a precise evaluation of the cold dark matter density [1]:

$$\Omega_c h^2 = 0.120 \pm 0.001 \; . \tag{1}$$

Constraints on new physics scenarios which propose dark matter candidates can therefore be obtained by comparing the computed dark matter density to the Planck value. The standard assumption to compute the dark matter density is to consider that dark matter particles are thermal relics, *i.e.* were in thermal equilibrium in the early Universe and we observe today only the surviving part. A second assumption is that there is a single thermal relic candidate contributing to the dark matter density, which is generally the case in BSM scenarios where dark matter particles have to be stable, electrically neutral and very weakly interacting.

With these assumptions, the relic density can be obtained by considering that all the new physics particles were originally in thermal equilibrium. Then the expansion of the Universe, which lowers the temperature, eventually breaks this equilibrium, and the evolution of the number densities of all the new particles can be obtained using Boltzmann equations, in which the expansion of the Universe introduces a friction-like term, and the collision terms include annihilations and co-annihilations of these new particles into SM particles. When the dark matter density is diluted enough so that the interactions become negligible, the relic density is frozen and becomes only diluted by the expansion of the Universe.

Comparing the obtained relic density to the very precise dark matter measurement, can lead to very strong constraints on new physics parameters. Several assumptions can nevertheless limit the constraining power of the relic density constraint as will be discussed in the following.

2.1.1. Higher order corrections The first uncertainties arise from the numerical calculations of the annihilation and co-annihilation cross sections. In the simplest cases the calculation of the relic density relies on a few decay channels, in the most compressed scenarios of the MSSM, more than 3000 channels can get involved, severely limiting the calculation speed of relic density. For this reason, the cross sections are generally considered at tree-level. Yet, in individual channels, higher-order corrections can lead to a 30% modification or more [2]. However, in most cases, the relic density calculated at tree-level differs by less than 10% from the one calculated at one-loop [3]. Therefore, in the general case, about a 10% uncertainty can be assigned to tree-level calculations of the relic density.

2.1.2. QCD equations of state A second limitation comes from the QCD equations of state. Indeed, computing the relic density requires the knowledge of the number of effective degrees of freedom of radiation, which lead to energy and entropy content of the Universe. While it was originally thought that the primordial plasma could be treated as an ideal gas above the QCD phase transition temperature, non-perturbative studies showed that at high temperature, the ideal gas approximation does not work, and different models for this plasma have been studied [4, 5], leading to different sets of QCD equations of state. The consequences on the relic density are, however, rather mild and can modify it by a few percent.

2.1.3. Early Universe properties In the usual calculation of relic density, the expansion of the Universe is considered to be dominated purely by the radiation density. This hypothesis can, however, be falsified in many extensions of the standard model of cosmology [6, 7]. Similarly, entropy injection or non-thermal production of dark matter particles can modify the relic density [8, 9]. These modifications of the standard model of cosmology can result in a change of the relic density by orders of magnitude, but are more likely to increase it. As a consequence, the uncertainties due to these effects are completely dominating the relic density calculation over the previous uncertainties.

2.2. Indirect detection

Dark matter particles hosted in galaxies are supposed to annihilate into SM particles to yield, after hadronisation and decay, nuclei, electrons, photons and neutrinos. Indirect detection experiments try to find an excess of those messengers on top of their astrophysical background. Even in the absence of signals, these experiments provide useful information about the nature of dark matter. The astrophysical background for antiparticle cosmic rays is composed of secondary particles, *i.e.* particles produced by the interaction of primary cosmic rays (mostly proton and helium nuclei) on the interstellar medium (mostly hydrogen and helium atoms). Hence, their background is feeble and relatively under control compared to other species. Antiprotons ($\bar{p}$) are the most abundant antinuclei in cosmic rays that could be produced by dark matter, and their spectral shape is distinguishable from the astrophysical background. For a dark matter mass larger than a few GeV, the flux of antiprotons features a cut off at the dark matter mass. The most accurate measurements of the $\bar{p}$ flux at the Earth was reported by the space-borne detector AMS-02 [10]. The discovery of an excess around 100 GeV was claimed a couple of years ago [11]. However, the astrophysical background suffers from theoretical uncertainties which make the significance of such an excess uncertain [12]. In any case, antiproton data provide strong constraints on the annihilation cross section of dark matter particles.

Compared to charged cosmic rays, gamma rays have the advantage of propagating straight ahead. This allows us to characterise the morphology of their sources and to observe regions where the dark matter particle density is expected to be large and to produce a sizeable flux. We consider here the results from the Fermi-LAT space-borne telescope, which covers the GeV energy range. Since the density of dark matter particles is peaked in the centre of the galaxy, the galactic centre is one of the best targets to look for a dark matter signal. Nevertheless, this region hosts important astrophysical activities, and it is difficult to estimate both the astrophysical background and foreground. On the other hand, dwarf spheroidal galaxies are considered as very interesting targets to look for a dark matter signal. Indeed, these systems are expected to: i) be dominated in mass by a DM component, ii) exhibit feeble stellar activities and have a low astrophysical background. Despite the fact that the dark matter distribution and concentration inside these objects is still under debate, they provide one of the best bounds on the average annihilating cross section $\langle \sigma v \rangle$.

2.2.1. Dark matter halo profiles Dark matter particles are assumed to be isotropically distributed in a spherical halo around the galactic centre, and several halo profiles are in particular considered: the NFW radial density profile of dark matter arising from cosmological simulations were parametrised by Navarro, Frenk and White [13]; the Einasto profile provides a better agreement with the latest simulations [14] and does not suffer from the central divergence of the NFW profile; the stellar activity occurring in the inner galaxy could sweep dark matter particles from the inner region, resulting in a core profile as observed in many galaxies, resulting in the Burkert profile [15].

2.2.2. Cosmic ray propagation As cosmic rays travel across the galaxy, they are affected by many processes as a result of their interactions with the galactic magnetic field. Moreover, cosmic rays can interact with the interstellar medium, leading to energy losses (including ionisation and Coulomb interactions) and their destruction. Finally, cosmic rays undergo the effect of the galactic wind produced by supernova remnant explosions in the galactic disc.

A semi-analytical method was used in [16] to derive the benchmark Min, Med, and Max propagation models. The Med model corresponds to the best fit to the boron over carbon (B/C) ratio, whereas the Min and Max sets of parameters define the lower and upper bounds for the primary $\bar{p}$ flux, consistent with the B/C ratio.

2.3. Direct detection

Direct dark matter searches aim at directly detecting WIMPs via tiny energy deposits when they scatter off target atomic nuclei in ultra-sensitive, low background detectors. No convincing dark matter signal has been detected so far, however, limits on the WIMP-nucleon cross section are set by comparing the measured differential recoil rate per unit detector mass to the theoretical rate.

Usually, the WIMP-nucleus cross section is decomposed into spin-independent (SI) and spin-dependent (SD) contributions in the zero momentum transfer limit. The SI form factors are experimentally well known from the study of elastic electronic scattering on nuclei and are reasonably well approximated by Helm form factors [17], while the SD form factors are obtained from nuclear shell model calculations [18].

The strongest limits on SI cross section, for $m_{DM} \gtrsim 10$ GeV, are given by xenon target experiments, and we consider in the following the results of XENON1T [19]. To constrain the SD WIMP-neutron cross section we consider the results from LUX [20].

2.3.1. Global and local dark matter densities All the experimental limits are calculated using the benchmark value $\rho_0 = 0.3$ GeV/cm^3 for the local DM density, but recent studies give a best fit value closer to 0.4 GeV/cm^3. The uncertainties on the local density value are still quite large, one of the main sources residing in the knowledge of the baryon density in the galaxy. There may also be a discrepancy between the value calculated from the study of the motion of nearby stars and the one calculated from a global fit of stellar dynamics over the galaxy, assuming a spherical dark matter halo. In our study, we will consider that the local DM density lies between 0.2 and 0.6 GeV/cm^3 (see [21] for a complete review) and will choose three different values to test the impact of those uncertainties on the exclusions in our sample of points: $\rho_0 = 0.2$, 0.4 and 0.6 GeV/cm^3.

2.3.2. Velocities Customarily, an isotropic Maxwellian distribution is assumed for the WIMP velocity distribution $f(\mathbf{v})$, with the Galactic disk rotation velocity v_{rot} being the most probable speed. It corresponds to the Standard Halo Model describing the dark matter halo as a non-rotating isothermal sphere [22]. The canonical value for v_{rot} is 220 km/s but it is believed that it can range from 200 to 250 km/s [23].
This velocity distribution is truncated at the escape velocity v_{esc} at which a WIMP can escape the galaxy potential well. Its value is subject to large uncertainties, $v_{esc} = 500 - 600$ km/s, with a benchmark value $v_{esc} = 544$ km/s [24]. However, for WIMP masses $m_{DM} > 10$ GeV, v_{min} is relatively low. The velocity distribution is then integrated over a large range of velocities and dR/dE_R is not sensitive to the tail of the distribution. Thus, the uncertainties on v_{esc} should not impact our analysis.

Other halo models have been proposed, such as the King Model, which describes the finite size of the halo and the gravitational interaction with ordinary matter in a more realistic way [25], or triaxial halo models [26]. In this study we will focus only on the uncertainties related to the Standard Halo Model, which is the most widely used in the literature.

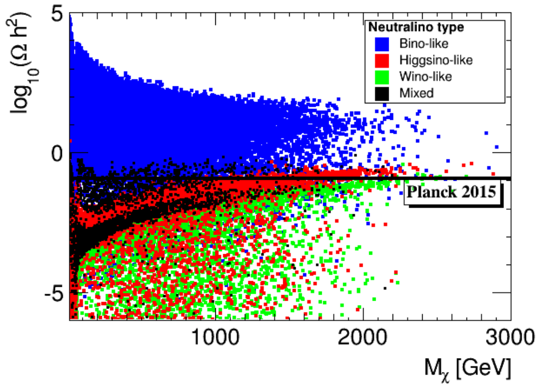

Figure 1: Neutralino relic density as a function of the neutralino 1 mass, for the different neutralino types. The central value of the Planck dark matter density is shown for comparison.

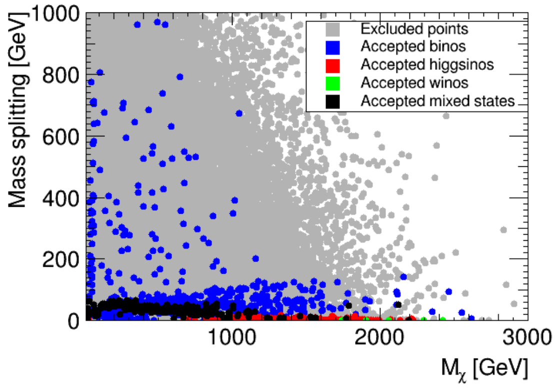

Figure 2: Points respecting the Planck relic dark matter density measurement in the mass splitting between the neutralino and the next lightest supersymmetric particle and the neutralino mass parameter plane.

3. Dark matter in the MSSM

3.1. MSSM Scans

We consider in this analysis the pMSSM, which is the most general R-parity and CP-conserving MSSM scenario with minimal flavour violation. The pMSSM points are generated with SOFTSUSY [27], with a flat random sampling over the 19 parameters with statistics of more than 20 million pMSSM points [28, 29]. All the masses are varied between 0 and 3 TeV, the trilinear couplings between -10 and 10 TeV, and $\tan\beta$ between 1 and 60. After checking the theoretical validity of each point, we impose that the neutralino be the lightest supersymmetric particle (LSP), as well as a light Higgs of mass between 122 and 128 GeV. We then apply different constraints from the dark matter and collider experiments, which are described below.

3.2. Dark matter constraints in the MSSM

We consider only model-points which have the lightest neutralino as the LSP and dark matter particle. In the following, the neutralino 1 (denoted χ) will be said to be bino-/wino-/Higgsino-like if it is composed of 90% of the bino-/wino-/Higgsino component, respectively, or mixed state otherwise. Bino-like χ are the most represented points in our sample, followed by the winos and Higgsinos, with an almost equal share of each component. The fraction of mixed states is negligible.

3.3. Relic density constraints

We first consider the relic density constraint. The value of the neutralino relic density is computed with SuperIso Relic [30–32]. In figure 1, the relic density is shown as a function of the neutralino 1 mass, for the different types [28]. Bino-like neutralinos 1 have in general large relic densities, above the Planck measurement. This can be explained by the smaller couplings of the binos with SM particles, which leads to smaller annihilation cross sections and therefore larger relic densities. On the other hand, the Higgsino-like χ give smaller relic densities which are close to the Planck measurements for χ masses around 1.3 TeV. The wino-like χ tend to have even smaller relic densities, and the Planck line is naturally reached for a mass of 2.7 TeV. The line at about 90 GeV in the figure corresponds to cross section enhancements through a Z-boson resonance, which lowers the relic density.

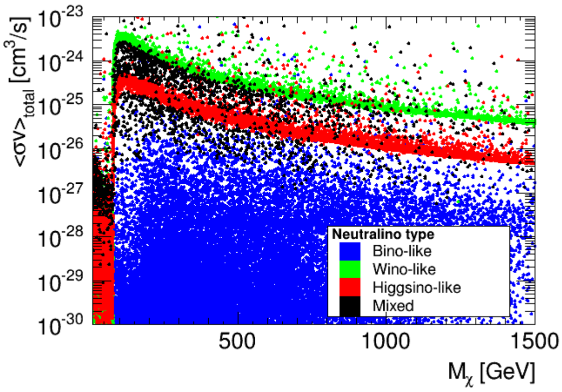

Figure 3: Total annihilation cross section as a function of the neutralino 1 mass for the different neutralino types.

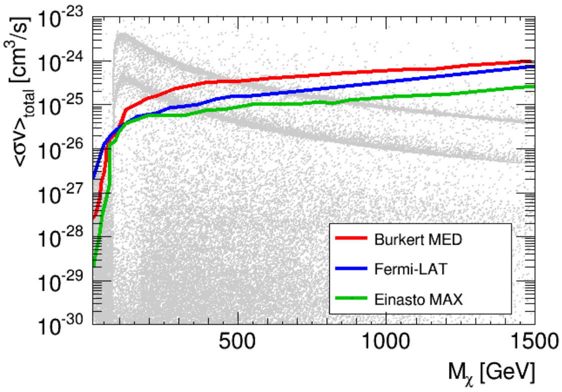

Figure 4: Points excluded by Fermi-LAT gamma ray and AMS-02 antiproton data in the total annihilation cross section vs. neutralino 1 mass parameter plane.

Imposing both the upper and lower relic density bounds generally leads to a selection of scenarios with co-annihilations, for which the mass splitting of the neutralino 1 with the next-to-lightest supersymmetric particle is small, or of scenarios where χ annihilations are enhanced through a resonance of the Z-boson or one of the neutral Higgs bosons. This is demonstrated in figure 2. The valid points require in general small mass splitting, apart from some spread binos with larger mass splittings, which have a heavy Higgs boson or Z-boson resonance. For the case of winos, the small mass splitting is due to a chargino with a mass very close to the χ mass. For the Higgsino case, both the chargino 1 and the neutralino 2 have masses close to the neutralino 1 mass.

As discussed in section 2.1, we consider only the upper bound of the Planck dark matter density interval, which favours light wino- and Higgsino-like χ, and bino-like χ with strong co-annihilations.

3.3.1. Indirect detection We consider the constraints from AMS-02 antiproton and Fermi-LAT gamma ray data, which probe specific dark matter annihilation channels. For both sets of constraints the most important parameters are the χ annihilation cross sections into specific channels. Annihilations to WW and $b\bar{b}$ are particularly interesting in the context of the pMSSM.

In figure 3, the total annihilation cross section times velocity $\langle\sigma v\rangle_{\rm tot}$ is shown as a function of the χ mass, for the different types. $\langle\sigma v\rangle_{\rm tot}$ is the sum of all the σv of the different channels. The wino- and Higgsino-like neutralino 1 regions form two separate strips. The different types of neutralinos 1 have specific main decay channels: binos annihilate mainly into $t\bar{t}$, $b\bar{b}$, and in a lesser extent into Wh, Zh and $\tau\tau$, Higgsinos into WW and ZZ, and winos into WW, when the decay channels are open. When the above-mentioned channels are closed because of a small χ mass, the χ mostly decays to $b\bar{b}$ and $\tau\tau$, and less frequently into $c\bar{c}$ and $s\bar{s}$, independently from their type [28]. As seen earlier, winos more strongly annihilate than the other χ types, followed by the Higgsinos. The binos, apart from the case of a resonant annihilation, are more weakly annihilating and are far below the experimental limits.

In figure 4, the exclusion by Fermi-LAT and AMS-02 is shown in the $\langle\sigma v\rangle_{\rm tot}$ vs. neutralino 1 mass parameter plane. In order to quantify the uncertainties related to indirect detection, we consider separately the most conservative limits, *i.e.* obtained using Burkert profile and MED propagation model, and the most stringent ones, *i.e.* using Einasto profile and

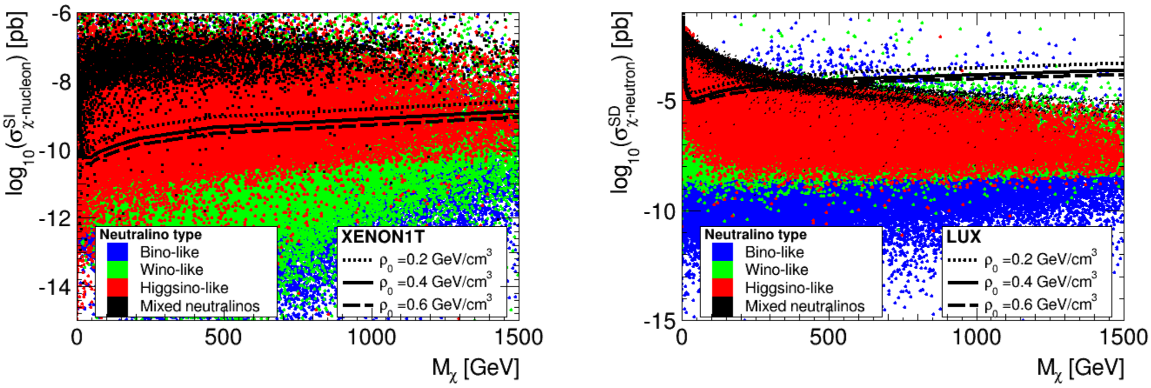

(a) (b)

Figure 5: Generalised (a) spin-independent and (b) spin-dependent neutralino scattering cross section as a function of the neutralino mass. The lines show the XENON1T (left) and LUX (right) 90% C.L. upper limit for three different values of the local dark matter density ρ_0.

Max propagation model. The conservative limits lead to the exclusion of neutralinos 1 with masses between 90 and 550 GeV, which are mainly wino-like. The stringent limits exclude points with χ masses between 0 and 850 GeV. In the small mass region, as well as for masses above 90 GeV, the stringent exclusion limit is strengthened by one order of magnitude in comparison to the conservative case. The stringent case excludes large zones of the wino strip, and of the Higgsino one in a lesser extent. AMS-02 alone brings very strong constraints in the stringent case, beyond the Fermi-LAT limits.

3.3.2. Direct detection Contrary to relic density and indirect detection, which mainly depend on the annihilation and co-annihilation cross sections, direct detection relies on the scattering cross section of neutralino 1 with nucleons. Direct detection is therefore complementary to indirect detection and relic density.

In figure 5, the generalised SI and SD WIMP-nucleon cross sections are shown as functions of the neutralino mass, for the different neutralino 1 types. Higgsinos are in general more strongly interacting than the winos, leading to larger cross sections. In order to assess the consequences of the uncertainties on the obtained constraints, the limits of the XENON1T and LUX experiments are superimposed, for three values of the local dark matter density, namely $\rho_0 = 0.2$, 0.4 and 0.6 GeV/cm^3. Between the conservative line corresponding to $\rho_0 = 0.2$ GeV/cm^3 and the most stringent limit obtained for $\rho_0 = 0.6$ GeV/cm^3, there is at most a factor 3 difference. While this is a large factor, in the context of pMSSM, it does not change much the excluded region, which contains mainly Higgsino-like neutralinos 1.

4. Modified cosmological scenarios

Big-Bang nucleosynthesis (BBN) provides constraints on the properties of the early Universe. Measurements of the nuclear abundances are in agreement with the assumption that the standard cosmological model is correct up to high energies (i.e., that the early Universe evolution is driven by radiation), which limits possible deviations from the standard cosmological model. However, probing cosmology at temperatures higher than tens of MeV is currently impossible. On the other hand, experiments at colliders, and particularly at the LHC, can probe the standard model of particle physics at the TeV scale. In the following we combine results from colliders and DM observations to set constraints on the cosmological properties of the Universe before BBN.

As an example we consider the cosmological scenario with a scalar field decaying into radiation and SUSY particles. We perform a scan over the reheating temperature T_{RH} and the initial scalar field density parametrised as the ratio between the scalar field density and the photon density at $T = T_{\rm init}$, $\kappa_\phi = \frac{\rho_\phi}{\rho_\gamma}(T = T_{\rm init})$, and calculate the relic density of different pMSSM points [33, 34]. We consider different values of the parameter $\eta = b\left(\frac{1\ \text{GeV}}{m_\phi}\right)$, where b is the branching ratio of the scalar field into WIMPs and m_ϕ the scalar field mass, in order to study the effect of non-thermal production of SUSY particles on the relic density. In each case we derive constraints on the scalar field parameters for our sample of pMSSM19 points so as to investigate the influence of the neutralino properties on the limits derived from the relic DM density.

We start integrating the Boltzmann equations at a temperature $T_{\rm init} = 40$ GeV. For our sample of pMSSM19 points, we use $T_{\rm init} = 1.5 \times T_{\rm fo}$, where $T_{\rm fo}$ is the freeze-out temperature in the standard cosmological model. These choices were made in order to reduce the computation time while starting the calculation sufficiently long before freeze-out and the decay of the scalar field.

4.1. Point with a large relic density

We first investigate the case where the neutralino has a relic density that is too large in the standard cosmological model.

As illustrated in figure 6(a), when T_{RH} is small, $\widetilde{\Sigma}^*$ can remain at its maximum during a large range of temperatures before its decrease due to the decay of the scalar field [33]. The neutralino and scalar field densities decrease during this period with a slope -5, as expected when $\widetilde{\Sigma}^*$ is at its maximum. Figure 6(b) shows that for a large value of T_{RH}, however, the fields are diluted over a smaller range of temperatures and the total decrease is reduced.

Figure 7 shows the effect of varying κ_ϕ and T_{RH} on the relic density. Points respecting the Planck constraints, which we will refer to as *accepted points*, lie along a thin line in the $\log_{10}(\kappa_\phi)/\log_{10}(T_{RH})$ plane. They follow a line of slope ~ 1 at small T_{RH} that changes slightly at $T_{RH} \sim 150$ MeV to a slope 1.5. This transition is the result of the quark/hadronic phase transition, which lowers the number of radiation degrees of freedom. In particular, below $T \sim 150$ MeV, pions become non-relativistic and no longer contribute to the radiation density. This feature is independent of the WIMP and scalar field properties, and is present in all the following results.

The line of accepted points becomes vertical at $T_{RH} \sim T_{\rm fo}$, which is to be expected when the scalar field decays completely during neutralino thermal equilibrium, as there is no possible modification of the relic density. Thus, we can derive a maximum value of the reheating temperature $T_{RH} \lesssim T_{\rm fo}$. One can also note that if $T_{RH} < T_{RH}^{\rm BBN\,lim} \sim 6$ MeV, the scalar field density is too large during BBN, and using AlterBBN [35, 36], we showed that the model is excluded by BBN constraints. This constraint is very general, as it is also independent of the WIMP properties, and thus applicable to any WIMP model. This limit gives us a lower bound for the reheating temperature, as well as a minimum value for the initial scalar field density κ_ϕ using $T_{RH} = T_{RH}^{\rm BBN\,lim}$. For our benchmark point we can deduce $\kappa_\phi \gtrsim 0.1$, but this minimum value will depend on the nature of the WIMP.

No enhancement of the relic density is possible when $\eta = 0$. At small T_{RH} and large κ_ϕ, where the scalar field density could have increased the freeze-out temperature via its relation with the Hubble parameter, and thereby increased the relic density, the densities are in fact already significantly reduced by dilution. Therefore, in order to increase the relic density, it is necessary to consider non-thermal production of the WIMP, i.e., $\eta > 0$. In our case, the region

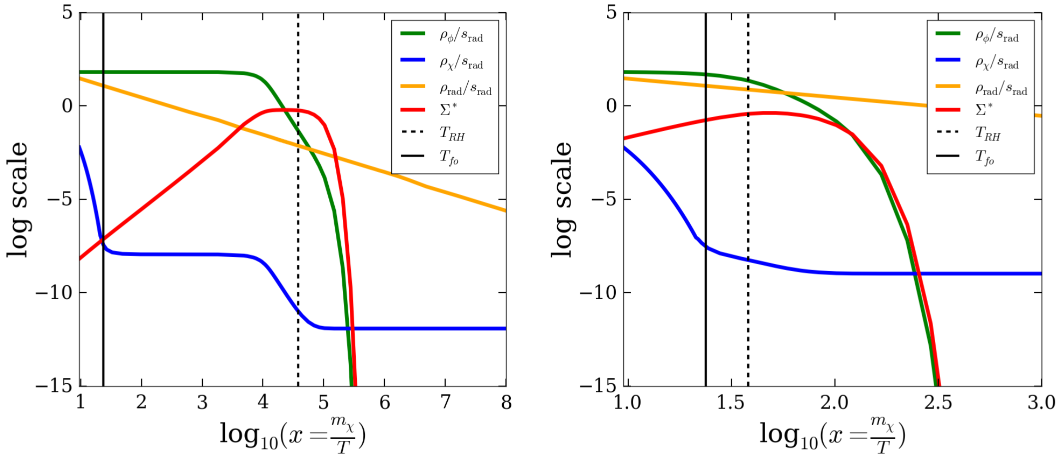

(a) (b)

Figure 6: The evolution of the scalar field, neutralino and radiation densities normalised to the radiation entropy density, and of the injection of entropy $\widetilde{\Sigma}^*$, as a function of $x = m_\chi/T$. (a): $T_{RH} = 0.01$ GeV, $\kappa_\phi = 100$, $T_{\rm init} = 40$ GeV. (b): $T_{RH} = 10$ GeV, $\kappa_\phi = 100$, $T_{\rm init} = 40$ GeV.

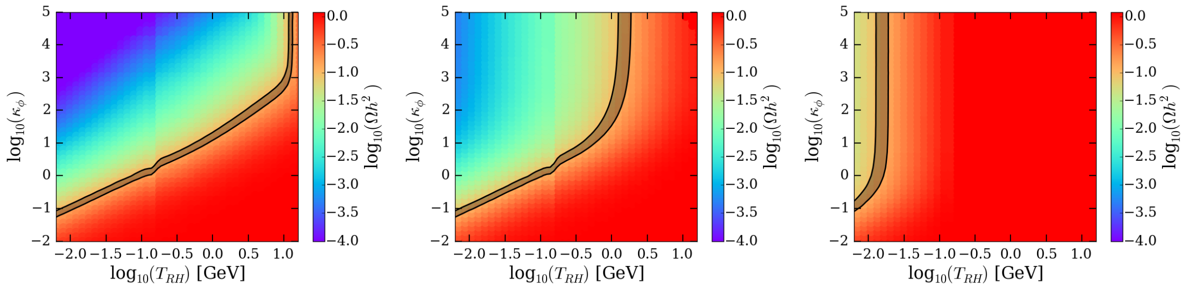

(a) $\eta = 0$ (b) $\eta = 10^{-12}$ (c) $\eta = 10^{-10}$

Figure 7: The effect of varying η on $\log_{10}(\Omega h^2)$ for the benchmark point with a large relic density, indicated by the colour code in the legend.

of interest will be at small T_{RH} and large κ_ϕ, where the relic density is strongly reduced by dilution. The scalar field decay into SUSY particles provides an additional contribution to the relic density, and the DM density measured by Planck may be reached with the appropriate value of η. We test four different values of η in figure 7, and notice that the larger η is the more the line of accepted points is shifted towards small T_{RH}.

In the limit of large κ_ϕ and small T_{RH}, we find that the evolution of the relic density with respect to η and T_{RH} can be approximated by:

$$\Omega h^2 \approx \eta \, (\alpha \, T_{RH} + \beta) \ , \tag{2}$$

where α and β are numerical factors that depend, *a priori*, on the WIMP properties. When η goes to zero, the relic density vanishes, which is expected since in this region of the parameter space the dilution due to the entropy injection is dominant, in the absence of non-thermal production. One can also note that the effects of the dilution and of the non-thermal production equilibrate in such a way that the above expression does not depend on κ_ϕ. For our benchmark

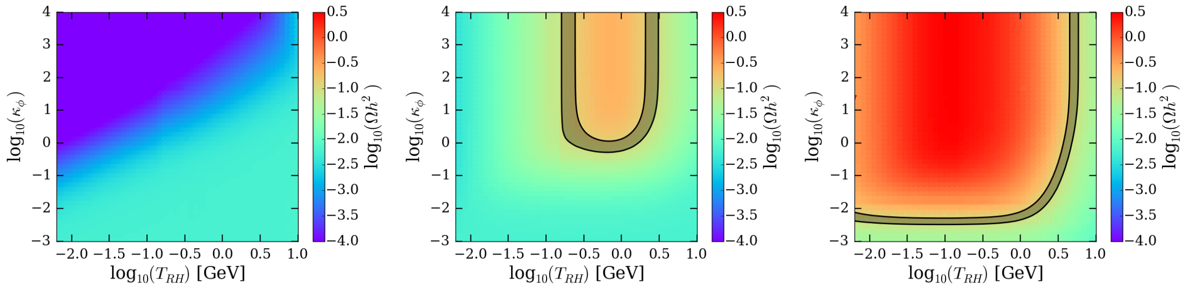

(a) $\eta = 0$ (b) $\eta = 10^{-11}$ (c) $\eta = 10^{-9}$

Figure 8: The effect of varying η on $\log_{10}(\Omega h^2)$ for a benchmark point with a small relic density, indicated by the colour code in the legend.

point we find that $\alpha \approx 7.68 \times 10^{10}$ GeV^{-1} and $\beta \approx 2.62 \times 10^7$. This parametrisation enables us to find the value of η required to get the correct relic density for a given reheating temperature. On the other hand, a maximum value of η can be calculated by considering the reheating temperature where the BBN constraints start excluding the model ($T_{RH}^{\rm lim} \approx 6 \times 10^{-3}$ GeV):

$$\eta_{\rm Max} = \frac{\Omega h^{2\,\rm upper\,lim}_{\rm DM}}{\alpha T_{RH}^{\rm lim} + \beta} \,. \tag{3}$$

For our benchmark point we calculate $\eta_{\rm Max} \approx 2.93 \times 10^{-10}$. Thus, in this scenario, the branching ratio into SUSY particles must be very small, which can be traced back to our choice of a scalar field with a substantial initial density. We note also that the variation in η does not modify the constraints on κ_ϕ and T_{RH} that we derived in the case $\eta = 0$. Strong constraints on the scalar field parameters can therefore be derived, namely 6 MeV $\lesssim T_{RH} \lesssim T_{\rm fo}$, $\kappa_\phi \gtrsim 0.1$ and $\eta \lesssim 2.93 \times 10^{-10}$.

4.2. Point with a small relic density

As discussed previously, no enhancement of the relic density is possible when only entropy injection is considered. Therefore, one needs to allow the scalar field to decay into BSM particles. We show in figure 8 the result of scans over T_{RH} and κ_ϕ for a benchmark point with three different values of η. In each scenario the region of accepted points forms a U shape in the κ_ϕ $/T_{RH}$ plane. The vertical right limit corresponds to $T_{RH} \sim T_{\rm fo}$, and does not move significantly as η increases. The vertical left limit, however, is shifted to the left along the T_{RH} axis and the horizontal limit is shifted downwards towards lower values of κ_ϕ. The constraints on T_{RH} that we deduced for the previous benchmark point hold also in this case: $T_{RH}^{\rm BBN\,lim} \lesssim T_{RH} \lesssim T_{\rm fo}$. However, it is difficult to find limits on κ_ϕ and η as stringent as the ones we found previously.

The largest effect is in the case where the scalar field decays entirely into BSM particles and not into radiation. Thus, if a decay produces two SUSY particles, for example, $b = 2$ and $m_\phi > 2m_\chi$, so $\eta < 1/m_\chi$. In such a case, all the SUSY particles produced by the scalar field decay, starting from the neutralino freeze-out, constitute an overall contribution to the relic density that has to be added to the value of the relic density in the standard model, i.e., $Y = Y_{\rm stand} + Y_\phi^{\rm T=T_{fo}}/m_\chi$. Therefore, one has a constraint on the scalar field density at freeze-out.

4.3. pMSSM19 sample

In the following we study how the constraints on the scalar field depend on the WIMP properties disregarding the case of a relic density that is too small, as the constraints deduced in this case

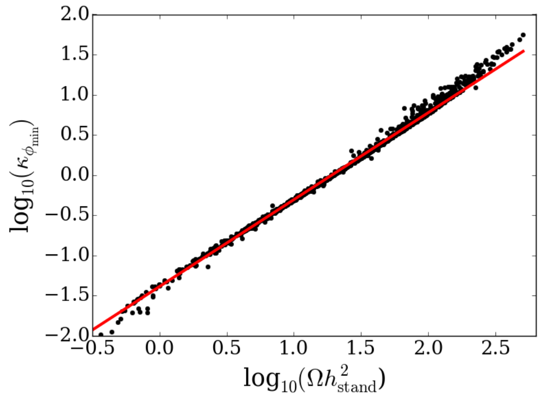

Figure 9: The values of κ_ϕ required to reduce the relic density to the measured DM density with $T_{RH} = T_{RH}^{\rm BBN\,lim}$ and $T_{\rm init} = 40$ GeV as a function of the relic density calculated in the standard model of cosmology.

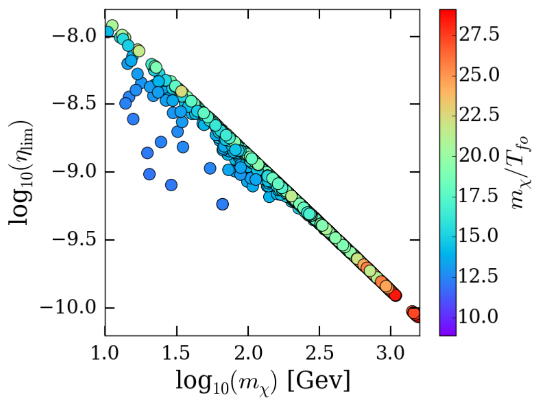

Figure 10: The maximum value of the parameter η for the pMSSM19 sample of points as a function of the neutralino mass. The values of $m_\chi/T_{\rm fo}$ are colour-coded as indicated in the legend.

already showed an explicit dependence on the freeze-out temperature and the relic density at freeze-out.

We focus on the points in our pMSSM19 sample that have a relic density that is too large in the standard cosmological model, which leaves us almost exclusively with bino-like neutralinos. We calculated the values of κ_ϕ that give the correct relic density at $T_{RH} = T_{RH}^{\rm BBN\,lim}$, as shown in figure 9, and find a very good correlation between the relic density calculated in the standard model and $\kappa_{\phi_{\min}}$.

The points in figure 9 follow a line of slope ~ 1. Thus, the minimum value of the initial scalar field density increases with the value of the relic density in the standard model. This can be understood because the larger the relic density at freeze-out is, the stronger the dilution for a given reheating temperature must be. The small scatter of the points at low relic density is due to numerical uncertainties alone, but we note a departure from this line at large $\Omega h^2_{\rm stand}$, when $\kappa_{\phi_{\min}} \gtrsim 1$. With a scalar field density of this order of magnitude, there is also a modification of the Hubble parameter, which advances freeze-out. This mechanism tends to increase the relic density, while the entropy injection decreases it. Overall, the dilution has a stronger effect, but a larger scalar field density is required to decrease the relic density down to the measured DM density.

Next, we calculate the maximum value of η and find a clear dependence on the WIMP mass, as seen in figure 10. Indeed, the scalar field produces a fraction b of SUSY particles, which contributes as $m_\chi \times b$ to the WIMP mass density. Therefore, the larger m_χ is, the more the relic density will be increased for a given value of η, and the smaller the maximum value of η will be. At first approximation, the maximum value of η is inversely proportional to the WIMP mass. However, another mechanism is at play: for the same neutralino mass, the larger $T_{\rm fo}$ is, the larger the neutralino density at the freeze-out temperature is, and thus the smaller η must be in order to reach the correct relic density. As $T_{{\rm fo}_{\rm stand}} \approx m_\chi/20$, we can express a linear relation between $\eta_{\rm lim}$ and m_χ. However, as shown in figure 10, when $T_{\rm fo}$ departs from this approximation towards larger values, the second mechanism becomes more important, and we see a departure from the linear relation between m_χ and $\eta_{\rm lim}$. This happens for neutralino masses smaller than ~ 100 GeV in our sample of points. In any case, η must be very small, of the order of $\sim 10^{-10}$ – 10^{-9}.

5. Conclusion

The BBN constraints currently constitute the earliest probe of the primordial Universe. The pre-BBN period is largely unconstrained, and many phenomena could have modified the standard cosmological scenario. We studied the impact of dark matter direct and indirect detections, in conjunction with relic density constraints, on the phenomenological MSSM with neutralino dark matter, and addressed in some detail the consequences of the related uncertainties. Furthermore, we discussed the case of modified cosmological scenarios and showed that a decaying cosmological scalar field can modify the relic density by orders of magnitude, showing that the relic density is very sensitive to the properties of the early Universe. Other possible phenomena, such as quintessence, phase transitions, moduli, etc., can lead to similar conclusions.

If new particles are discovered in particle physics experiments, and the properties of the underlying scenario are determined, comparing the relic density to the measured dark matter density would allow us to probe the early Universe and, if there is a discrepancy, could lead to the discovery of new cosmological phenomena, as was illustrated here.

References

[1] Aghanim N *et al.* (Planck) 2018 (*Preprint* `1807.06209`)
[2] Baro N, Boudjema F and Semenov A 2008 *Phys. Lett.* **B660** 550–560 (*Preprint* `0710.1821`)
[3] Baro N, Boudjema F, Chalons G and Hao S 2010 *Phys. Rev.* **D81** 015005 (*Preprint* `0910.3293`)
[4] Hindmarsh M and Philipsen O 2005 *Phys. Rev.* **D71** 087302 (*Preprint* `hep-ph/0501232`)
[5] Drees M, Hajkarim F and Schmitz E R 2015 *JCAP* **1506** 025 (*Preprint* `1503.03513`)
[6] Kamionkowski M and Turner M S 1990 *Phys. Rev.* **D42** 3310–3320
[7] Arbey A and Mahmoudi F 2008 *Phys. Lett.* **B669** 46–51 (*Preprint* `0803.0741`)
[8] Moroi T and Randall L 2000 *Nucl. Phys.* **B570** 455–472 (*Preprint* `hep-ph/9906527`)
[9] Arbey A and Mahmoudi F 2010 *JHEP* **05** 051 (*Preprint* `0906.0368`)
[10] Aguilar M *et al.* (AMS) 2016 *Phys. Rev. Lett.* **117** 091103
[11] Cuoco A, Krämer M and Korsmeier M 2017 *Phys. Rev. Lett.* **118** 191102 (*Preprint* `1610.03071`)
[12] Giesen G, Boudaud M, Génolini Y, Poulin V, Cirelli M, Salati P and Serpico P D 2015 *JCAP* **1509** 023 (*Preprint* `1504.04276`)
[13] Navarro J F, Frenk C S and White S D M 1996 *Astrophys. J.* **462** 563–575 (*Preprint* `astro-ph/9508025`)
[14] Navarro J F, Ludlow A, Springel V, Wang J, Vogelsberger M, White S D M, Jenkins A, Frenk C S and Helmi A 2010 *Mon. Not. Roy. Astron. Soc.* **402** 21 (*Preprint* `0810.1522`)
[15] Burkert A 1996 *IAU Symp.* **171** 175 [Astrophys. J.447,L25(1995)] (*Preprint* `astro-ph/9504041`)
[16] Delahaye T, Lineros R, Donato F, Fornengo N and Salati P 2008 *Phys. Rev.* **D77** 063527 (*Preprint* `0712.2312`)
[17] Lewin J D and Smith P F 1996 *Astropart. Phys.* **6** 87–112
[18] Klos P, Menéndez J, Gazit D and Schwenk A 2013 *Phys. Rev.* **D88** 083516 [Erratum: Phys. Rev.D89,no.2,029901(2014)] (*Preprint* `1304.7684`)
[19] Aprile E *et al.* (XENON) 2017 *Phys. Rev. Lett.* **119** 181301 (*Preprint* `1705.06655`)
[20] Akerib D S *et al.* (LUX) 2017 *Phys. Rev. Lett.* **118** 251302 (*Preprint* `1705.03380`)
[21] Read J I 2014 *J. Phys.* **G41** 063101 (*Preprint* `1404.1938`)
[22] Freese K, Frieman J A and Gould A 1988 *Phys. Rev.* **D37** 3388–3405
[23] McMillan P J and Binney J J 2010 *Mon. Not. Roy. Astron. Soc.* **402** 934 (*Preprint* `0907.4685`)
[24] Smith M C *et al.* 2007 *Mon. Not. Roy. Astron. Soc.* **379** 755–772 (*Preprint* `astro-ph/0611671`)
[25] Chaudhury S, Bhattacharjee P and Cowsik R 2010 *JCAP* **1009** 020 (*Preprint* `1006.5588`)
[26] Evans N W, Carollo C M and de Zeeuw P T 2000 *Mon. Not. Roy. Astron. Soc.* **318** 1131 (*Preprint* `astro-ph/0008156`)
[27] Allanach B C 2002 *Comput. Phys. Commun.* **143** 305–331 (*Preprint* `hep-ph/0104145`)
[28] Arbey A, Boudaud M, Mahmoudi F and Robbins G 2017 *JHEP* **11** 132 (*Preprint* `1707.00426`)
[29] Robbins G, Mahmoudi F, Arbey A and Boudaud M 2017 *PoS* **EPS-HEP2017** 082 (*Preprint* `1710.03658`)
[30] Arbey A and Mahmoudi F 2010 *Comput. Phys. Commun.* **181** 1277–1292 (*Preprint* `0906.0369`)
[31] Arbey A and Mahmoudi F 2011 *Comput. Phys. Commun.* **182** 1582–1583
[32] Arbey A, Mahmoudi F and Robbins G 2019 *Comput. Phys. Commun.* **239** 238–264 (*Preprint* `1806.11489`)
[33] Arbey A, Ellis J, Mahmoudi F and Robbins G 2018 *JHEP* **10** 132 (*Preprint* `1807.00554`)
[34] Arbey A, Ellis J, Mahmoudi F and Robbins G 2018 *PoS* **ICHEP2018** 035 (*Preprint* `1811.12764`)
[35] Arbey A 2012 *Comput. Phys. Commun.* **183** 1822–1831 (*Preprint* `1106.1363`)
[36] Arbey A, Auffinger J, Hickerson K P and Jenssen E S 2018 (*Preprint* `1806.11095`)